

Electronic Supplementary Information (ESI)

Sustainable Development of Graphitic Carbon Nanosheets from Plastic Wastes with Efficient Photothermal Energy Conversion for Enhanced Solar Evaporation

Marliyana Aizudin^{a†}, Ronn Goei^{b†}, Amanda Jiamin Ong^b, Yong Zen Tan^c, Shun Kuang Lua^c, Rafeeqe Poolamuri Pottammel^d, Hongbo Geng^e, Xing-Long Wu^f, Alfred Iing Yoong Tok^{b**}, and Edison Huixiang Ang^{a*}

^aNatural Sciences and Science Education, National Institute of Education, Nanyang Technological University, Singapore 637616, Singapore.

^bSchool of Materials Science and Engineering, Nanyang Technological University, Singapore 639798, Singapore.

^cSchool of Chemical and Biomedical Engineering, Nanyang Technological University, Singapore 637459, Singapore

^dDepartment of Chemistry, Indian Institute of Science Education and Research Thiruvananthapuram, India 695551, India.

^eSchool of Materials Engineering, Changshu Institute of Technology, Changshu, Jiangsu, 215500, P.R. China

^fFaculty of Chemistry, Northeast Normal University, Changchun, Jilin, 130024, P.R. China

[†]These authors contribute equally to this work.

*Main corresponding author email: edison.ang@nie.edu.sg; (+65)-67903831

**Co-corresponding author email: MIYTok@ntu.edu.sg; (+65)-6790 4935

Experimental Section

Materials and chemicals

Common household plastic waste such as plastic bag (PB), laundry detergent bottle (LB), and Tupperware container (TC) made of different plastic recycling grade such as low-density polyethylene (LDPE), high-density polyethylene (HDPE) and polypropylene (PP) were utilised as starting materials. Concentrated sulphuric acid, (H_2SO_4) 98% was purchased from Merck and used as received. Sodium chloride (NaCl) was purchased from Sigma Aldrich. Deionized (DI) water with an electrical resistivity of 18.2 M Ω cm was obtained from a TTL-30C Ultrapure Water Generator. Air-laid paper was purchased from Kleenex.

Fabrication of 2D g-CNS materials: Firstly, plastic waste consisting of PB, LB and TC were individually cut into small pieces. Next, the cut-up pieces of PB were placed in a Teflon vessel where it was immersed in concentrated sulfuric acid and then secured with a Teflon cap. Subsequently, the Teflon vessel was heated in oven at 110 °C for a duration of 12 h and cooled to ambient temperature naturally after completion. Upon opening the Teflon vessel, the as-obtained sulfonated carbon black flakes were collected then rinsed with deionised water via centrifugation for several times in order to remove any unreacted acid before drying in the oven at 60 °C overnight. Next, the sulfonated carbon black materials were carbonized in a tubular furnace at 900 °C for 2 h under Argon atmosphere at a flow rate of 200 mL min⁻¹. The heating and cooling rates were 10 °C min⁻¹. After carbonization, the samples were grounded homogeneously using a pestle and mortar to produce 2D g-CNS_{PB} sample. The above synthesis steps were repeated on the LB and TC plastic wastes to produce 2D g-CNS_{LB} and 2D g-CNS_{TC} samples, respectively.

Characterizations of 2D g-CNS materials: X-ray diffraction (XRD) patterns were collected using a Smart Lab X-ray diffractometer (Shimadzu XRD-6000) operated using a monochromate Cu $K\alpha$ radiation source ($\lambda = 0.154$ nm) and the samples were measured from 20 ° to 65 °. Water contact angle measurement was carried out on a micro-optical contact angle measurement (Attension Theta) by using a 4 μL droplet of water as an indicator. The X-ray photoelectron spectroscopy (XPS) studies were conducted using a Krato Axis Ultra spectrometer with a monochromatic Al $K\alpha$ excitation source ($h\nu = 1486.71$ eV). The studies were carried out in an ultrahigh vacuum chamber with a base pressure below 2.66×10^{-7} Pa at room temperature. The binding energies were calibrated against C 1s core level at 284.8 eV for the adventitious carbon as reference. All peaks were fitted and deconvoluted using XPS Peak41 software. Raman spectra were collected using a Nanophoton Ramantouch microscope with a 532 nm laser. Field-emission scanning electron microscopy (FESEM) was conducted using a JEOL JSM-6700F Analysis Station and the elemental mapping analyses were analysed using an Oxford Instrument energy dispersive X-ray spectroscopy (EDX). Transmission microscope (TEM) were conducted using a TEM JEOL 2100F, with an accelerating voltage 200 kV with integrated selected area electron diffraction (SAED) detector. The morphology of the 2D g-CNS was observed using atomic force microscopy (AFM, Park System NX10) instrument. Attenuated Total Reflection (ATR) Fourier transform infrared (FTIR) spectroscopy (Perkin Elmer instrument, Spectrum 100) was utilised for the FTIR spectra. The absorption spectrum was investigated using a UV-Vis-NIR spectrophotometer (Agilent Varian Cary 5000). The infrared mappings and temperature distributions were captured using the thermal imaging camera (FLIR CAT S61). N_2 adsorption/desorption isotherm analyses were performed using Quanta chrome Autosorb-1 system instrument analyser at 77 K using liquid N_2 . Prior to the measurement, the sample materials undergo outgassing at 300 °C for 24 h in order to remove any adsorbed species from the sample. Thermal conductivity values were conducted using the C-Therm Trident, Multiple Transient Plane Source (MTPS) in accordance with ASTM D7984.

Evaluation of solar-vapor generation performances: Desired amount of 2D g-CNS sample was homogeneously dispersed in the deionised water and sonicated for 10 min. The 2D g-CNS_{PB} suspension was then vacuum filtered on the air-laid paper to form 2D g-CNS_{PB} photothermal layer. To create the solar evaporator device, the 2D g-CNS photothermal layer was supported on a 2 cm-thick polystyrene (PS) foam and placed on the simulated seawater in a beaker (see Fig. S16). The solar evaporation experiment the fabricated solar evaporator were conducted at a lab-made, online, real time measurement system that consists of a solar light simulator (Toption TOPX-300), an analytical balance (Mettler Toledo) and a computer to record the time-dependent mass change of water due to the vapour generation by placing on an analytical balance under the photochemical lamp. Light intensity was measured by an optical power meter (TENMARS TM-207) for one-sun solar illumination. During each test, the room temperature was maintained at 19-22 °C and the humidity was ranged from 15-20%.

S1. To determine PTCE using equation (3) in main text, the total enthalpy of vaporisation¹ can be calculated as follows:

$$h_{LV} = \lambda + C\Delta T \quad (S1)$$

where λ is the latent heat of vaporisation,² C is the specific heat capacity of water (4.2 kJ kg⁻¹ K⁻¹), and ΔT denotes the temperature increase of the water. The latent heat of vaporisation of 2D g-CNS_{PB}, 2D g-CNS_{LB}, 2D g-CNS_{TC} solar absorbers and control is 2417.9 kJ kg⁻¹, 2419.1 kJ kg⁻¹, 2424.1 kJ kg⁻¹ and 2438.1 kJ kg⁻¹, respectively. Therefore, the total enthalpy of vaporisation, h_{LV} , is 2459.9 kJ kg⁻¹ (35 °C), 2459.0 kJ kg⁻¹ (34.5 °C), 2455.2 kJ kg⁻¹ (32.4 °C) and 2444.4 kJ kg⁻¹ (26.5 °C) which corresponds to 2D g-CNS_{PB}, 2D g-CNS_{LB}, 2D g-CNS_{TC} solar absorbers and control, respectively.

S2. Thermal heat losses of solar-vapor generation performance³⁻⁶: As known, the heat loss of water evaporation processes consists of three parts, radiation, convection, and conduction. The calculation details of the following heat losses are shown below:

1. Radiation

The heat radiation loss was calculated through Stefan-Boltzmann equation:

$$\phi = \varepsilon A\sigma(T_1^4 - T_2^4) \quad (S2)$$

where ϕ represents heat flux, ε is the emissivity, and emissivity in the water evaporation processes is supposed to have a maximum emissivity of 1. A is the effective evaporation surface area (ca. 962 mm²). σ is the Stefan-Boltzmann constant (the value is 5.67 x 10⁻⁸ W m⁻² K⁻⁴). T_1 is the surface temperature of the as-prepared 2D g-CNS solar absorber after stable steam generation under one-sun illumination, and T_2 represents ambient temperature. According to the Equation S2, the radiation heat flux of 2D g-CNS_{PB}, 2D g-CNS_{LB}, and 2D g-CNS_{TC} solar evaporators are 63.1 W m⁻², 59.8 W m⁻² and 46.0 W m⁻², respectively. Therefore, the calculated heat radiation loss of 2D g-CNS_{PB}, 2D g-CNS_{LB}, and 2D g-CNS_{TC} solar evaporators are 6.3%, 6.0% and 4.6%, respectively.

2. Convection

The convection heat loss can be calculated by Newton's law of cooling as follows:

$$Q = hA\Delta T \quad (S3)$$

where Q is the convection heat flux, h represents the convection heat transfer coefficient, which is approximately $5 \text{ W m}^{-2} \text{ K}^{-1}$. and A is the effective evaporation surface area (ca. 962 mm^2). ΔT is the difference between surface temperature of the as-prepared 2D g-CNS solar absorbers and the ambient temperature. Consequently, the convection heat loss of 2D g-CNS_{PB}, 2D g-CNS_{LB}, and 2D g-CNS_{TC} solar evaporators was calculated through Equation S3, and the values are 5.0%, 4.8%, and 3.7%, respectively.

3. Conduction

The conduction heat loss is due to the heat that was transferred from the as-prepared materials to water, which can be calculated by the following equation:

$$q = kA \frac{(T_1 - T_2)}{L} \quad (S4)$$

where q is the heat transfer by conduction, k is the thermal conductivity of the 2D g-CNS solar absorber, A is the surface area of heat transfer (ca. 962 mm^2), T_1 and T_2 are the temperature differences between surface temperature of the as-prepared 2D g-CNS solar absorber after steady state temperature and the ambient temperature and L is the thickness of the photothermal layer supported on PS foam (21 mm). The thermal conductivities of 2D g-CNS_{PB}, 2D g-CNS_{LB} and 2D g-CNS_{TC} solar absorbers are $0.059 \text{ W m}^{-1} \text{ K}^{-1}$, $0.061 \text{ W m}^{-1} \text{ K}^{-1}$ and $0.044 \text{ W m}^{-1} \text{ K}^{-1}$, respectively.

Consequently, according to Equation S4, the calculated conduction heat loss of 2D g-CNS_{PB}, 2D g-CNS_{LB} and 2D g-CNS_{TC} solar evaporators are 2.8%, 2.7% and 1.6%, respectively. Hence, the heat loss of 2D g-CNS_{PB} solar evaporator in the water evaporation processes is 14.1%, including radiation (6.3%), convection (5.0%) and conduction (2.8%), while the heat loss of 2D g-CNS_{LB} solar evaporator is 13.5%, including radiation (6.0%), convection (4.8%) and conduction (2.7%) and lastly, the heat loss of 2D g-CNS_{TC} solar evaporator is 9.9%, including radiation (4.6%), convection (3.7%) and conduction (1.6%).

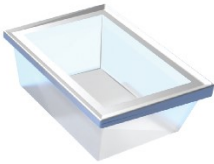
| Types of Plastic Waste | Chemical Structure |
|--|--|
| <p data-bbox="359 241 512 271">Plastic Bag (PB)</p>  | <p data-bbox="855 241 1118 271">Low-density polyethylene</p> $ \begin{array}{c} \text{CH}_3 \\ \\ \text{CH}_2 \\ \\ \text{---C---} \left[\text{---C---C---} \right]_n \text{---C---} \\ \qquad \qquad \qquad \qquad \\ \text{H} \qquad \qquad \text{H}_2 \qquad \text{H}_2 \qquad \text{H} \qquad \text{H}_2 \\ \\ \text{CH}_2 \\ \\ \text{CH}_2 \\ \\ \text{CH}_3 \end{array} $ |
| <p data-bbox="288 591 584 620">Laundry Detergent Bottle (LB)</p>  | <p data-bbox="855 591 1118 620">High-density polyethylene</p> $ \text{---C---} \left[\text{---C---C---} \right]_n \text{---C---} $ |
| <p data-bbox="300 925 572 954">Tupperware Container (TC)</p>  | <p data-bbox="911 925 1062 954">Polypropylene</p> $ \left[\text{---C---} \begin{array}{c} \text{H}_2 \\ \\ \text{C} \end{array} \text{---} \begin{array}{c} \text{H} \\ \\ \text{CH}_3 \end{array} \right]_n $ |

Fig. S1 Schematic illustration of the types of plastic wastes consisting of plastic bag (PB), laundry detergent bottle (LB) and Tupperware container (TC) along with their chemical structures.

Table S1. A summary of the solar steam generation capabilities of certain recently reported photothermal materials under one-sun illumination.

| Photothermal Materials | Category | Water Evaporation Rate (kg m ⁻² h ⁻¹) | PTCE (%) | Reference |
|--|-------------------|--|-----------|------------------|
| rGO-MWCNT | Carbonaceous | 1.22 | 80 | [7] |
| GO film | Carbonaceous | 1.45 | 80 | [8] |
| CB/PMMA-PAN membrane | Carbonaceous | 1.3 | 72 | [9] |
| F-wood/CNTs | Carbonaceous | 0.95 | 65 | [10] |
| Flame-treated wood | Carbonaceous | 1.05 | 72 | [11] |
| Carbonized mushrooms | Carbonaceous | 1.47 | 78 | [12] |
| RGO-SA-CNT aerogel | Carbonaceous | 1.39 | 83 | [13] |
| Carbon particles | Carbonaceous | 0.96 | 70 | [14] |
| Black Ag nanostructures | Inorganic/ceramic | 1.38 | 68 | [15] |
| AuFs/silica gel | Inorganic/ceramic | 1.36 | 85 | [16] |
| AuNP/PBONF | Inorganic/ceramic | 1.42 | 83 | [17] |
| GO/Ti ₃ C ₂ T _x | Inorganic/ceramic | 1.34 | 85 | [18] |
| PDA@MXene | Inorganic/ceramic | 1.28 | 85 | [19] |
| Al-TiO | Inorganic/ceramic | 1.03 | 78 | [20] |
| TiNO | Inorganic/ceramic | 1.33 | 84 | [21] |
| Carbonized membrane (CM) | Commercial | 0.96 | 66 | [22] |
| 2D g-CNS_{PB} | 2D g-CNS | 1.50 | 99 | This work |
| 2D g-CNS _{LB} | | 1.41 | 94 | |
| 2D g-CNS _{TC} | | 1.30 | 86 | |

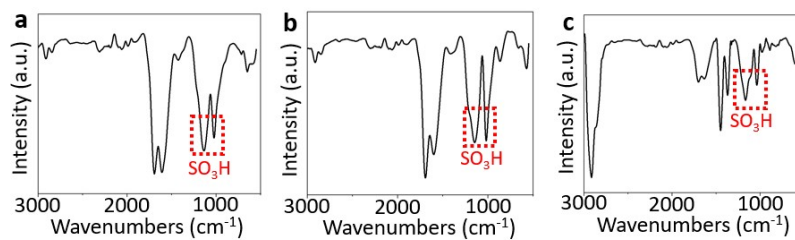


Fig. S2 ATR-FTIR spectra of sulfonated carbon black precursors (a) s-CB_{PB} (b) s-CB_{LB} (c) s-CB_{TC} samples.

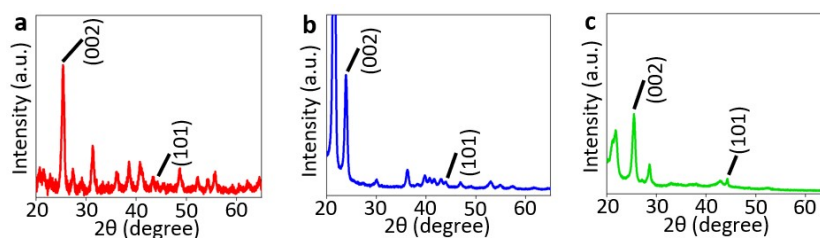


Fig. S3 XRD patterns of (a) s-CB_{PB}, (b) s-CB_{LB} and (c) s-CB_{TC} samples. The XRD diffraction peaks of 26.1° (002) and 45° (101) represent the hexagonal graphitic carbon (JCPDS No. 56-0159).



Fig. S4 Photographs of 2D g-CNS_{PB}, 2D g-CNS_{LB} and 2D g-CNS_{TC} samples (left to right) disperse uniformly in ethanol solvent after ultrasonication for 15 min and left undisturbed for a day.

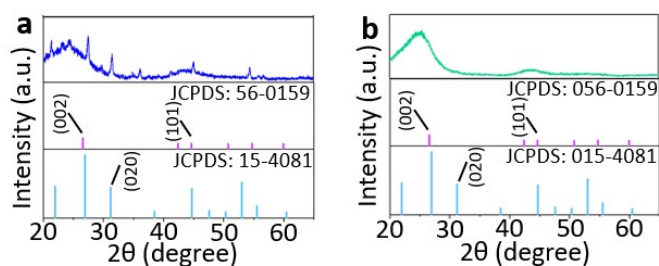


Fig. S5 XRD patterns of (a) 2D g-CNS_{LB} and (b) 2D g-CNS_{TC} samples.

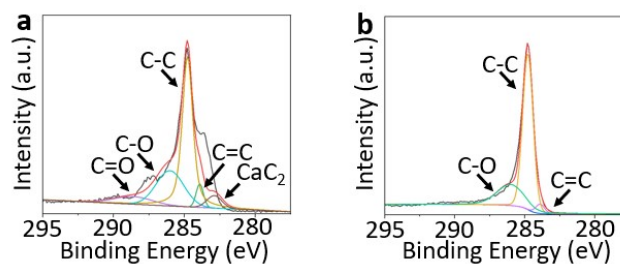


Fig. S6 XPS spectra of (a) 2D g-CNS_{LB} and (b) 2D g-CNS_{TC} samples.

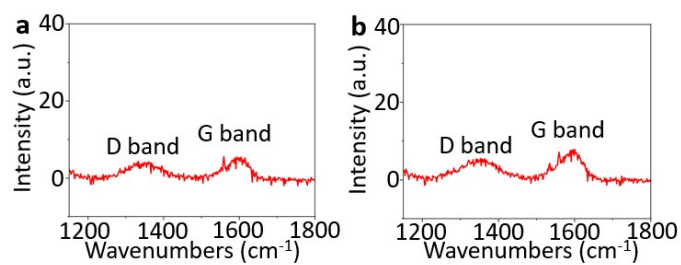


Fig. S7 Raman spectrums of (a) 2D g-CNS_{LB} and (b) 2D g-CNS_{TC} samples.

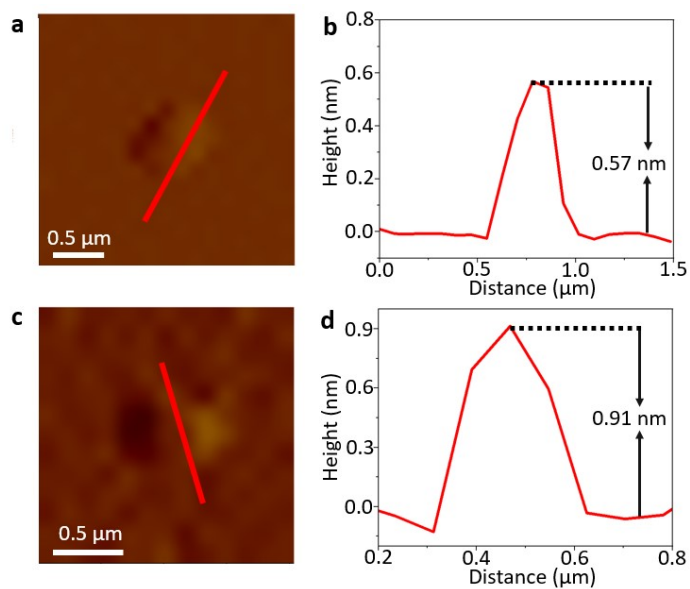


Fig. S8 (a) AFM image with its (b) height profile of 2D g-CNS_{LB} sample. (c) AFM image with its (d) height profile of 2D g-CNS_{TC} sample.

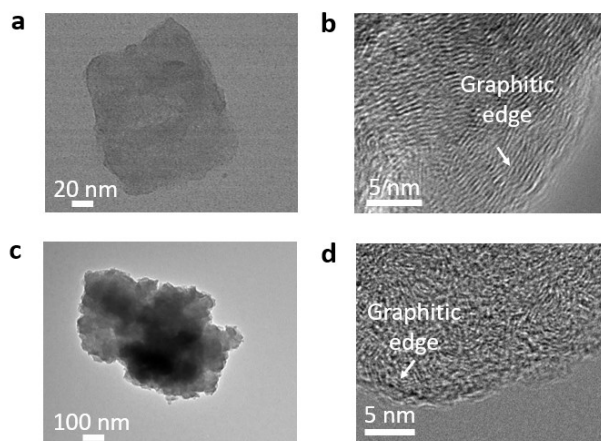


Fig. S9 (a) Low-magnification and (b) high-magnification TEM images of 2D g-CNS_{LB} sample. (c) Low-magnification and (d) high-magnification TEM images of 2D g-CNS_{TC} sample.

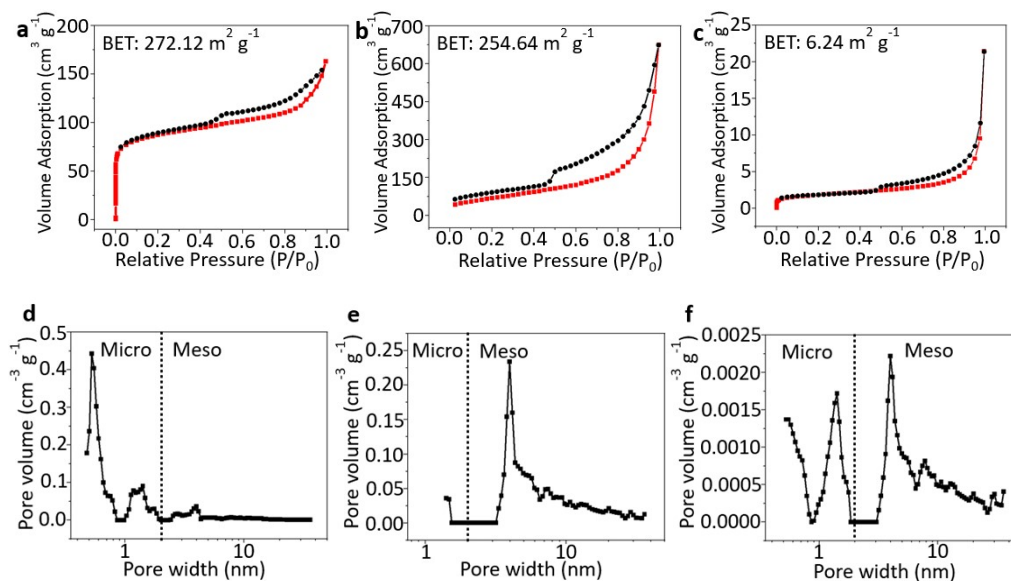


Fig. S10 N₂ adsorption-desorption isotherm of (a) 2D g-CNS_{PB}, (b) 2D g-CNS_{LB} and (c) 2D g-CNS_{TC} samples. NLDFT pore size distribution of (d) 2D g-CNS_{PB}, (e) 2D g-CNS_{LB} and (f) 2D g-CNS_{TC} samples in microporous and mesoporous regions.

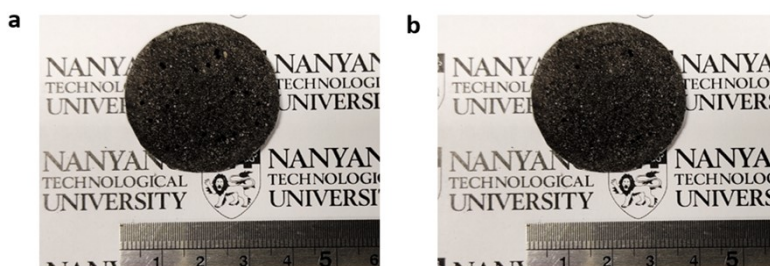


Fig. S11 Photographs of (a) 2D g-CNS_{LB} and (b) 2D g-CNS_{TC} solar absorbers on air-laid paper support.

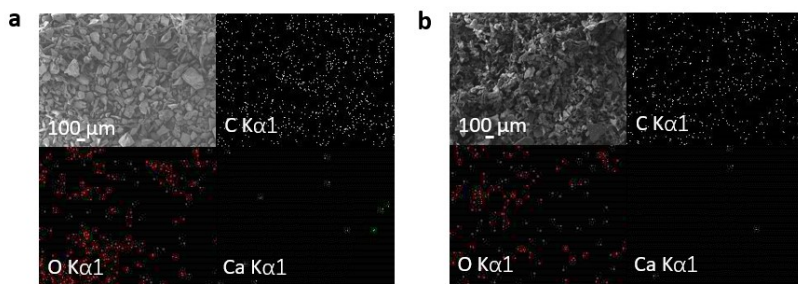


Fig. S12 FESEM image with the corresponding EDX mapping images of (a) 2D g-CNS_{LB} and (b) 2D g-CNS_{TC} solar absorbers on air-laid paper support.

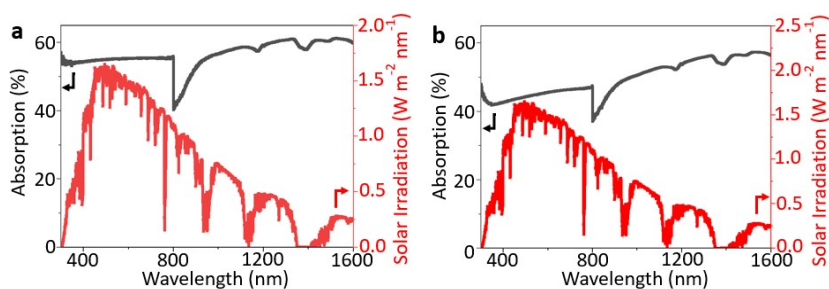


Fig. S13 UV-Vis-NIR spectra of (a) 2D g-CNS_{LB} (b) 2D g-CNS_{TC} solar absorbers using mass optimization, with the AM 1.5 solar irradiance as a reference (red).

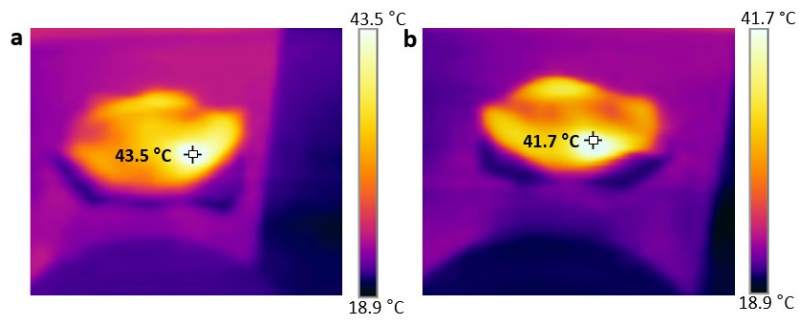


Fig. S14 Thermal images of (a) 2D g-CNS_{LB} and (b) 2D g-CNS_{TC} photothermal layer under air.

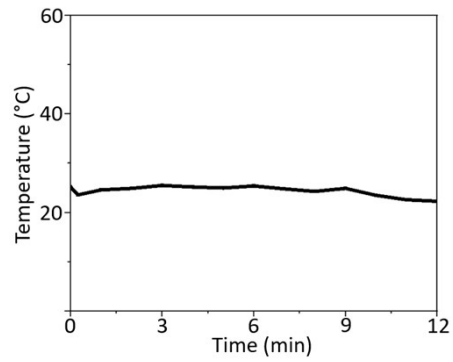


Fig. S15 Surface temperature recording of control experiment against time under air.



Fig. S16 Photograph of the solar evaporator setup.

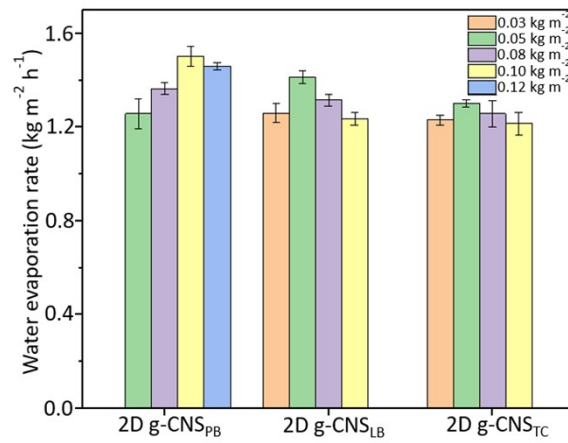


Fig. S17 Optimum mass determination of 2D g-CNS_{PB}, 2D g-CNS_{LB} and 2D g-CNS_{TC} samples at various mass loadings of 0.03, 0.05, 0.08, 0.1 and 0.12 kg m⁻², respectively, against the water evaporation rate.

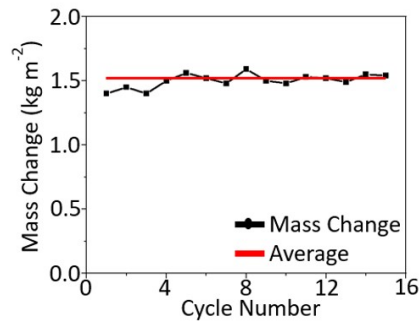


Fig. S18 Cycle stability of 2D g-CNS_{PB} solar evaporator under one-sun illumination.

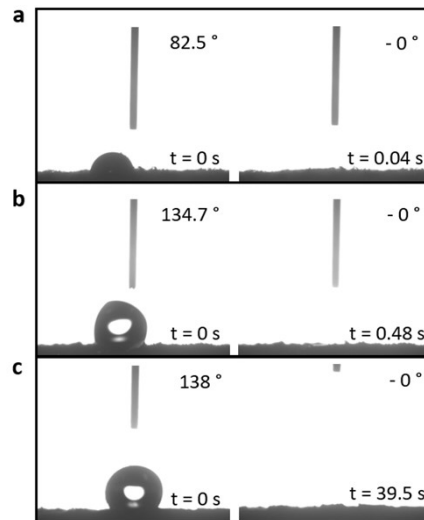


Fig. S19 Dynamic water contact angle measurement for (a) 2D g-CNS_{PB} (b) 2D g-CNS_{LB} and (c) 2D g-CNS_{TC} photothermal layers using optimum mass loadings. The image at 0 s was captured when the water droplet rests on the surface and stopped until no change in the droplet size.

Table S2 Atomic percentages (at%) of 2D g-CNS_{PB}, g-CNS_{LB} and g-CNS_{TC} samples based on XPS results.

| Samples | at% | | | | |
|------------------------|-----|-----|------|------|------------------|
| | C=C | C=O | C-C | C-O | CaC ₂ |
| 2D g-CNS _{PB} | 5.4 | 8.2 | 38.7 | 31.2 | 16.6 |
| 2D g-CNS _{LB} | 4.8 | 8.0 | 55.2 | 26.8 | 5.2 |
| 2D g-CNS _{TC} | 3.6 | - | 69.8 | 26.5 | - |

Table S3 2D g-CNS_{PB}, g-CNS_{LB} and g-CNS_{TC} samples based on Raman results.

| Samples | I _G /I _D ratio |
|------------------------|--------------------------------------|
| 2D g-CNS _{PB} | 1.32 |
| 2D g-CNS _{LB} | 1.25 |
| 2D g-CNS _{TC} | 1.24 |

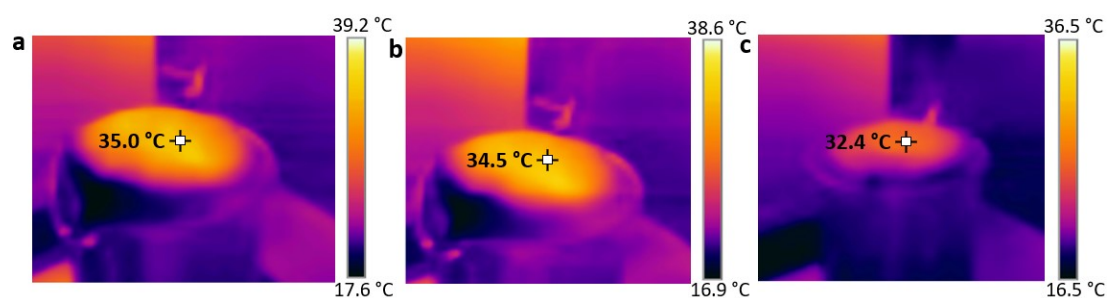


Fig. S20 Thermal images of (a) 2D g-CNS_{PB} (b) 2D g-CNS_{LB}, and (c) 2D g-CNS_{TC} photothermal layers on water surface under one-sun illumination.

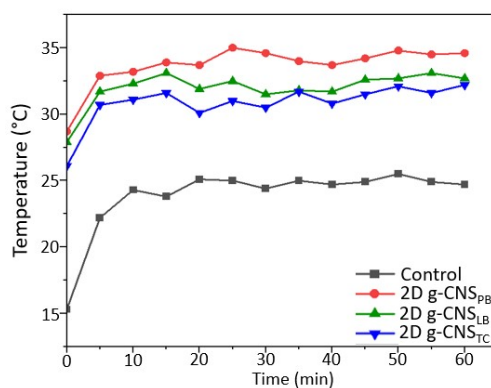


Fig. S21 Surface temperature recordings of 2D g-CNS_{PB}, 2D g-CNS_{LB} and 2D g-CNS_{TC} photothermal layers on water surface against time under one-sun illumination.

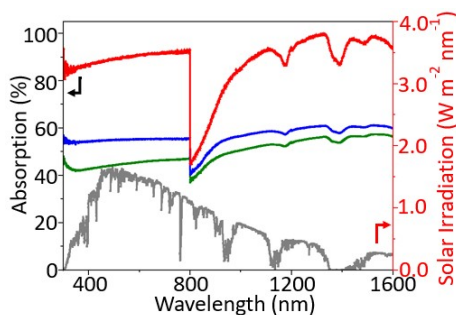


Fig. S22 UV-Vis-NIR spectra of 2D g-CNS_{PB} (red), 2D g-CNS_{LB} (blue) and 2D g-CNS_{TC} (green) solar absorbers using equal mass loading of 0.08 kg m⁻², with the AM 1.5 solar irradiance as a reference (grey).

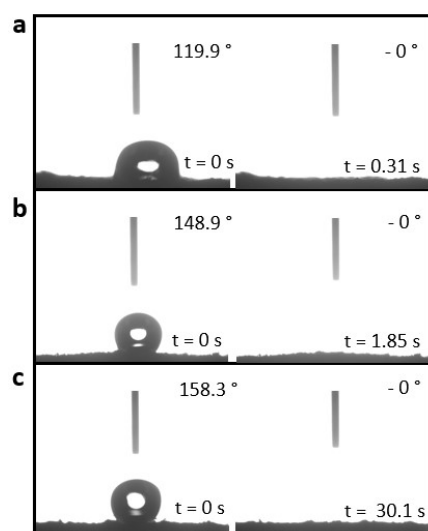


Fig. S23 Dynamic water contact angle measurement for (a) 2D g-CNS_{PB} (b) 2D g-CNS_{LB} and (c) 2D g-CNS_{TC} photothermal layers using equal mass loadings of 0.08 kg m⁻². The image at 0 s was captured when the water droplet rests on the surface and stopped until no change in the droplet size.

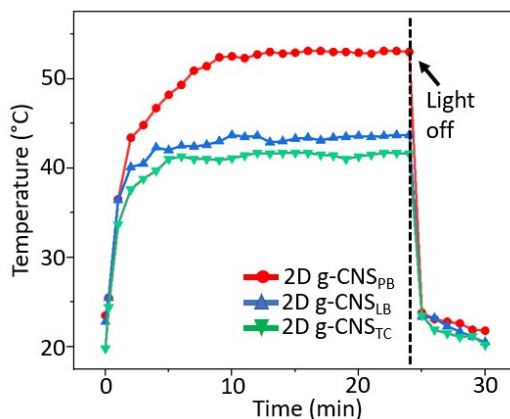


Fig. S24 Surface temperature versus time plot of 2D g-CNS_{PB}, 2D g-CNS_{LB} and 2D g-CNS_{TC} samples under one-sun illumination.

References

1. P. Mu, W. Bai, Y. Fan, Z. Zhang, H. Sun, Z. Zhu, W. Liang and A. Li, *Journal of Materials Chemistry A*, 2019, **7**, 9673-9679.
2. L. Zhang, Z. Xu, L. Zhao, B. Bhatia, Y. Zhong, S. Gong and E. N. Wang, *Energy & Environmental Science*, 2021, **14**, 1771-1793.
3. L. Zhu, M. Gao, C. K. N. Peh and G. W. Ho, *Materials Horizons*, 2018, **5**, 323-343.
4. C. Song, L. Hao, B. Zhang, Z. Dong, Q. Tang, J. Min, Q. Zhao, R. Niu, J. Gong and T. Tang, *Science China Materials*, 2020, **63**, 779-793.
5. H. Ghasemi, G. Ni, A. M. Marconnet, J. Loomis, S. Yerci, N. Miljkovic and G. Chen, *Nature Communications*, 2014, **5**, 4449.
6. M. Gao, L. Zhu, C. K. Peh and G. W. Ho, *Energy & Environmental Science*, 2019, **12**, 841-864.
7. Y. Wang, C. Wang, X. Song, S. K. Megarajan and H. Jiang, *Journal of Materials Chemistry A*, 2018, **6**, 963-971.
8. X. Li, W. Xu, M. Tang, L. Zhou, B. Zhu, S. Zhu and J. Zhu, *Proc Natl Acad Sci U S A*, 2016, **113**, 13953-13958.
9. W. Xu, X. Hu, S. Zhuang, Y. Wang, X. Li, L. Zhou, S. Zhu and J. Zhu, *Advanced Energy Materials*, 2018, **8**, 1702884.

10. M. Xie, J. Qian, Y. Li, H. Yang, J. Qu, X. Hu and Q. Mao, *Appl. Opt.*, 2021, **60**, 4930-4937.
11. G. Xue, K. Liu, Q. Chen, P. Yang, J. Li, T. Ding, J. Duan, B. Qi and J. Zhou, *ACS Applied Materials & Interfaces*, 2017, **9**, 15052-15057.
12. N. Xu, X. Hu, W. Xu, X. Li, L. Zhou, S. Zhu and J. Zhu, *Advanced Materials*, 2017, **29**, 1606762.
13. X. Hu, W. Xu, L. Zhou, Y. Tan, Y. Wang, S. Zhu and J. Zhu, *Advanced Materials*, 2017, **29**, 1604031.
14. S. Liu, C. Huang, X. Luo and Z. Rao, *Applied Thermal Engineering*, 2018, **142**, 566-572.
15. J. Chen, J. Feng, Z. Li, P. Xu, X. Wang, W. Yin, M. Wang, X. Ge and Y. Yin, *Nano Letters*, 2018, **19**, 400-407.
16. M. Gao, C. K. Peh, H. T. Phan, L. Zhu and G. W. Ho, *Advanced Energy Materials*, 2018, **8**, 1800711.
17. M. Chen, Y. Wu, W. Song, Y. Mo, X. Lin, Q. He and B. Guo, *Nanoscale*, 2018, **10**, 6186-6193.
18. X. Zhao, L.-M. Peng, C.-Y. Tang, J.-H. Pu, X.-J. Zha, K. Ke, R.-Y. Bao, M.-B. Yang and W. Yang, *Materials Horizons*, 2020, **7**, 855-865.
19. X. Zhao, X.-J. Zha, L.-S. Tang, J.-H. Pu, K. Ke, R.-Y. Bao, Z.-y. Liu, M.-B. Yang and W. Yang, *Nano Research*, 2020, **13**, 255-264.
20. L. Yi, S. Ci, S. Luo, P. Shao, Y. Hou and Z. Wen, *Nano Energy*, 2017, **41**, 600-608.
21. C. Chang, M. Liu, L. Pei, G. Chen, Z. Wang and Y. Ji, *AIP Advances*, 2021, **11**, 045228.
22. X. Lin, M. Yang, W. Hong, D. Yu and X. Chen, *Frontiers in Materials*, 2018, **5**, 1-8.